

a result of net compressive forces operating on the hot early crust over a convective downwelling, and (iii) the hemispheric surficial and interior dichotomy as due to lateral transport of material during differentiation. The model is in conflict with the simple geophysical argument that the high Rayleigh number of a 500-km-thick magma ocean will promote small-scale turbulent convection rather than global-scale convection, but the current degree of ignorance of nature, let alone behavior of the actual lunar magma ocean, may not make this a tightly binding constraint.

The distribution of elevations on the moon is distinctly irregular, and the near side and far side differ both in mean elevation and shape of the hypsographic curve. There is a correlation between topography and composition, and five hypsographic units have been defined with differing compositional characteristics. Two of these units, the South Pole–Aitken Basin and the nearside mare basalts, are clearly the result of impact and volcanism, respectively. The lack of extensive mare basalt fill in the South Pole–Aitken Basin, despite the thin crust in this region, suggests hemispheric compositional asymmetry in the deep lunar interior. Early giant impact can explain many of the observed characteristics, but not the deep-interior compositional asymmetry. Primordial differentiation processes can explain all of the observed compositional and hypsographic characteristics but suffer from the lack of an understood mechanism for causing global- rather than small-scale lateral convective transport.

#### REFERENCES AND NOTES

1. W. M. Kaula *et al.*, *Proc. Lunar Planet. Sci. Conf.* **5**, 3049 (1974).
2. M. T. Zuber and D. E. Smith, *Science* **266**, 1839 (1994).
3. This data set was constructed by averaging all pixels in each charge-coupled device (CCD) camera image to a single pixel. Each "image-pixel" was then calibrated for camera gain and offset and integration time. The data were then projected into simple cylindrical coordinates. Each image was photometrically corrected with the Lommel-Selliger photometric function. Finally, an empirical phase function was derived from a portion of the far side highlands between the longitudes of the eastern South Pole–Aitken Basin and the western portion of the Orientale Basin.
4. A. E. Metzger *et al.*, *Proc. Lunar Planet. Sci. Conf.* **8**, 949 (1977).
5. P. D. Spudis and P. A. Davis, *J. Geophys. Res.* **91** (suppl.), E85 (1986).
6. P. A. Davis and P. D. Spudis, *ibid.* **92** (suppl.), E387 (1987).
7. The albedo and the ratio of a band near 1  $\mu\text{m}$  and a band on the continuum, usually around 560 or 750 nm, are typically used to infer the relative amounts of mafic material in mature lunar soils in multispectral images. However, these parameters are not unambiguously coupled to the mafic content of lunar soils. The albedo of a mature soil is due to the reflectance of the minerals making up the source rock, the reflectance of impact glasses produced by micrometeorite bombardment, and the amount of reduced iron in the soil in the form of submicroscopic blebs

which are produced by the reduction of  $\text{Fe}^{2+}$  in minerals by solar wind-implanted hydrogen. Mafic minerals in source rocks vary widely in their reflectances, and each mineral is subject to the reduction process at different rates. Work by E. M. Fischer and C. M. Pieters (*J. Geophys. Res.*, in preparation) shows that there is no correlation between Al and visible albedo for highland areas overflowed by Apollo x-ray spectrometers. The ratio of a band near 1  $\mu\text{m}$  to a continuum band is not directly coupled to mafic content in that it decreases in value with increasing abundance of mafic minerals but increases in value with maturity, but the specific mineralogy of the source dictates the relative importance of these properties. Thus, these parameters must be used with care when specifying the composition.

8. B. R. Hawke, P. D. Spudis, G. J. Taylor, P. G. Lucey, C. A. Peterson, *Meteoritics* **28**, 361 (1993).
9. A. S. McEwen *et al.*, *Science* **266**, 1858 (1994).
10. C. M. Pieters, *Rev. Geophys.* **24**, 557 (1986).
11. P. H. Warren and J. T. Wasson, *Proc. Lunar Planet. Sci. Conf.* **11**, 431 (1980).
12. S. C. Solomon, *ibid.* **6**, 1021 (1975).
13. D. E. Wilhelms, *U.S. Geol. Surv. Prof. Pap.* **1348** (1987); J. A. Wood, *Moon* **8**, 73 (1973).

14. J. W. Head and L. Wilson, *Geochim. Cosmochim. Acta* **56**, 2155 (1992).
15. Y. A. Surkov, *Proc. Lunar Planet. Sci. Conf.* **12B**, 1377 (1981).
16. G. Ryder and J. A. Wood, *ibid.* **8**, 655 (1977); M. P. Charette *et al.*, *ibid.*, p. 1049; P. D. Spudis *et al.*, *J. Geophys. Res.* **90** (suppl.), C197 (1985).
17. C. G. Andre and P. L. Strain, *J. Geophys. Res.* **88** (suppl.), A544 (1983); P. H. Schultz and P. D. Spudis, *Proc. Lunar Planet. Sci. Conf.* **10**, 2899 (1979).
18. G. Ryder and P. D. Spudis, *Geochim. Cosmochim. Acta* (suppl.) **12**, 353 (1980).
19. R. Phillips, personal communication.
20. We would like to thank the efforts of the Navy Research Laboratory, the Lawrence Livermore National Laboratory, the Ballistic Missile Defense Organization, the U.S. Air Force, the National Aeronautics and Space Administration, and the numerous private contractors who made Clementine happen. This is School for Ocean and Earth Sciences and Technology contribution number 3759, Hawaii Institute of Geophysics and Planetology contribution number 785, and Lunar Planetary Institute contribution number 849.

10 August 1994; accepted 1 November 1994

## Clementine Observations of the Aristarchus Region of the Moon

Alfred S. McEwen,\* Mark S. Robinson, Eric M. Eliason, Paul G. Lucey, Tom C. Duxbury, Paul D. Spudis

Multispectral and topographic data acquired by the Clementine spacecraft provide information on the composition and geologic history of the Aristarchus region of the moon. Altimetry profiles show the Aristarchus plateau dipping about 1° to the north-northwest and rising about 2 kilometers above the surrounding lavas of Oceanus Procellarum to the south. Dark, reddish pyroclastic glass covers the plateau to average depths of 10 to 30 meters, as determined from the estimated excavation depths of 100- to 1000-meter-diameter craters that have exposed materials below the pyroclastics. These craters and the walls of sinuous rilles also show that mare basalts underlie the pyroclastics across much of the plateau. Near-infrared images of Aristarchus crater reveal olivine-rich materials and two kilometer-sized outcrops of anorthosite in the central peaks. The anorthosite could be either a derivative of local magnesium-suite magmatism or a remnant of the ferroan anorthosite crust that formed over the primordial magma ocean.

The Clementine mission has provided global multispectral mapping of the entire moon in 11 bandpasses (415, 750, 900, 950, 1000, 1100, 1250, 1500, 2000, 2600, and 2780 nm) and altimetry profiles from about -75° to +75° latitude (1). In this report, we present preliminary interpretations of a small portion of these observations, from the Aristarchus region (latitude 18°N to 32°N, longitude 42°W to 57°W).

The geologic and compositional diversity of the Aristarchus region (2–7) and evidence for active emission of volatiles from Aristarchus crater (8–9) have led to pro-

posals for surface exploration and resource exploitation (10–12). The 170 km by 200 km Aristarchus plateau, an elevated crustal block just west of the outer ring of the Imbrium Basin (Fig. 1), includes the densest concentration of sinuous rilles known on the moon. Most of these rilles begin at distinctive "cobra-head" craters (or irregular depressions), the probable source vents for a reddish dark mantling deposit (DMD) that blankets the entire elevated plateau; the DMD probably consists of volatile-rich pyroclastic glass (4, 13, 14). The plateau is embayed on all sides by mare basalts of Oceanus Procellarum. The well-preserved Copernican impact crater Aristarchus, 42 km in diameter, lies on the southeastern edge of the plateau. The Aristarchus plateau may have been the source region for a significant portion of the mare basalts of Oceanus Procellarum (15). The movement and temporary storage of a large volume of

A. S. McEwen, M. S. Robinson, E. M. Eliason, U.S. Geological Survey, Flagstaff, AZ 86001, USA.  
P. G. Lucey, Planetary Geoscience Division, University of Hawaii, Honolulu, HI 96822, USA.  
T. C. Duxbury, Jet Propulsion Laboratory, Pasadena, CA 91109, USA.  
P. D. Spudis, Lunar and Planetary Institute, Houston, TX 77058, USA.

\* To whom correspondence should be addressed.

magma may have profoundly altered the mineralogy of the country rock; highland materials in the Aristarchus region are much richer in mafic minerals (olivine and high-Ca pyroxene) than are typical lunar highlands (4, 16).

Altimetry profiles indicate that the Aristarchus plateau is a tilted slab sloping downward to the north-northwest and rising about 2 km above Oceanus Procellarum on its southern margin (Fig. 2). Previous topographic data (17) indicated that the plateau dipped predominantly to the west and that the plateau rose nearly 5 km above Oceanus Procellarum.

We have completed preliminary calibrations and mosaicking of a subset of the Clementine images covering the Aristarchus region. The entire region has been mosaicked with images from three bandpasses of the ultraviolet-visible (UVVIS) camera, centered at 415, 750, and 1000 nm (Fig. 3), and a north-south strip of images has been processed from four bandpasses of the near-infrared (NIR) camera (1100, 1250, 1500, and 2000 nm). Spatial resolutions range from 90 to 160 m/pixel in the UVVIS images, and 135 to 240 m/pixel in the NIR images. The best previous digital multispectral imaging of this region has a resolution of ~2000 m/pixel (18). Color ratios serve to cancel out the dominant brightness variations of the scene, which are controlled by albedo variations and topographic shading, thus enhancing and isolating the color differences related to mineralogy and soil maturity (19). In Fig. 3 we present a color-ratio composite with the 750/415-nm, 750/1000-nm, and 415/750-nm ratios controlling the red, green, and blue, respectively.

Once calibrations and processing of the Clementine data are complete, we will pro-

duce quantitative mineralogic maps. At this time, however, our compositional interpretations of the color-ratio composite (Fig. 3) are based on correlations with Earth-based telescopic spectra (4). Exposures of gabbroic highland materials are blue, the glassy Fe<sup>2+</sup>-rich pyroclastics or DMD (4, 13) are deep red, fresh exposures of mare basalt are yellowish or greenish, and mature mare soils are purplish or reddish [corresponding to "blue" and "red" mare units (20)]. Albedo variations have also been very useful for our interpretations. Aristarchus ejecta consists of mixtures of highland, mare, DMD, and impact melt (5, 6); thus, it has a complex variety of colors and albedos. With this data set, basic compositional units can be mapped at a much higher spatial resolution than has been previously possible.

The mare versus highland color signatures of craters of various diameters can be used to reconstruct the crude stratigraphy of the plateau. All craters larger than ~2-km diameter on the plateau have excavated predominantly highland gabbroic materials (including Herodotus D, where we now see that the southeastern wall is mostly highland material). The transient cavity of simple craters may have a depth-to-diameter ratio of ~1/3, but the maximum depth of excavation may be as little as ~0.10 times the diameter (21). On this basis, we estimate that the maximum thickness of mare materials on the plateau is 200 to 600 m. Radar returns indicate that the Aristarchus DMD is at least 6 m deep (22). Colors indicative of mare basalt or highland materials can be seen (Fig. 3) in the interiors (but not in the ejecta) of many 100- to 500-m-diameter craters superimposed over the DMD. We interpret these crater colors as being due to different compositions rath-

er than to "immature" DMD, because (i) most researchers interpret the glassy materials in DMD as original volcanic ash or cinders rather than the products of micrometeoroid impacts (4, 13, 14); and (ii) Aristarchus secondary impacts on the DMD must have exposed immature DMD, yet the resulting color and albedo effects are minor. Therefore, given the expected excavation depths, we estimate an average DMD thickness of 10 to 30 m. A previous estimate of 50 to 100 m for its average thickness (3) was based on the sizes of nearly filled craters, but other processes, such as impact erosion and lava flows, may have filled these craters before deposition of DMD.

Mare basalts are common on the Aristarchus plateau. Previous geologic mapping (2, 3) indicated the possible presence of mare basalts over ~25% of the plateau, where the surface morphology is relatively smooth, and the remaining, hummocky terrains were interpreted as highland materials. Almost the entire plateau is covered by DMD or Aristarchus ejecta, and subsurface materials are seen only where exposed by superposed craters or on steep slopes. Except for a few large craters (diameter >10 km) and large mountain slopes such as Herodotus  $\chi$  (Fig. 1), these exposures have not been resolved by previous multispectral observations. The only previous spectral observation (4) indicating the presence of mare basalt on the plateau was for the crater Herodotus D, on the extreme northwest corner of the plateau (Fig. 1). The 100 m/pixel color mosaic (Fig. 3) reveals the subsurface composition in many locations in 100- to 1000-m-diameter craters and along the steep walls of sinuous rilles. The walls of Vallis Schröteri are composed mostly of mare basalt, rather than highland material as previously mapped (2, 3), ex-

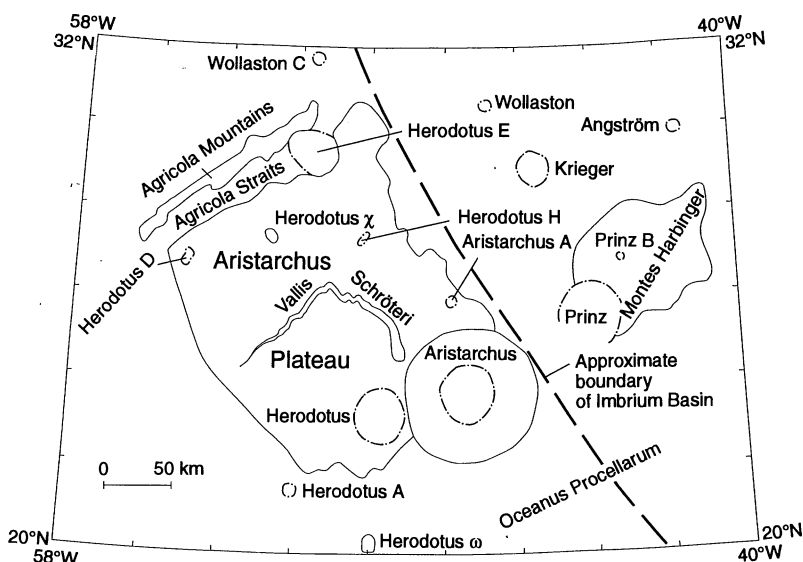


Fig. 1. Location map of the Aristarchus region. The dashed line indicates the approximate position of the outer ring of the Imbrium Basin (26).

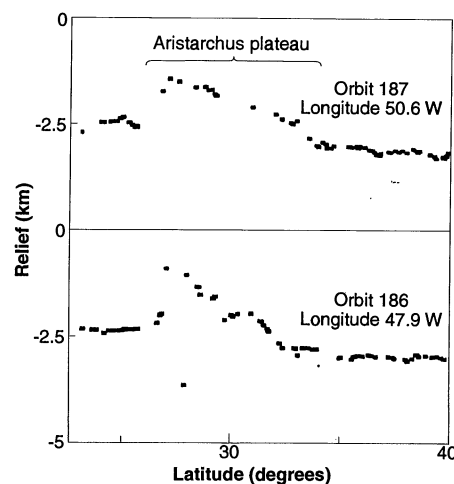
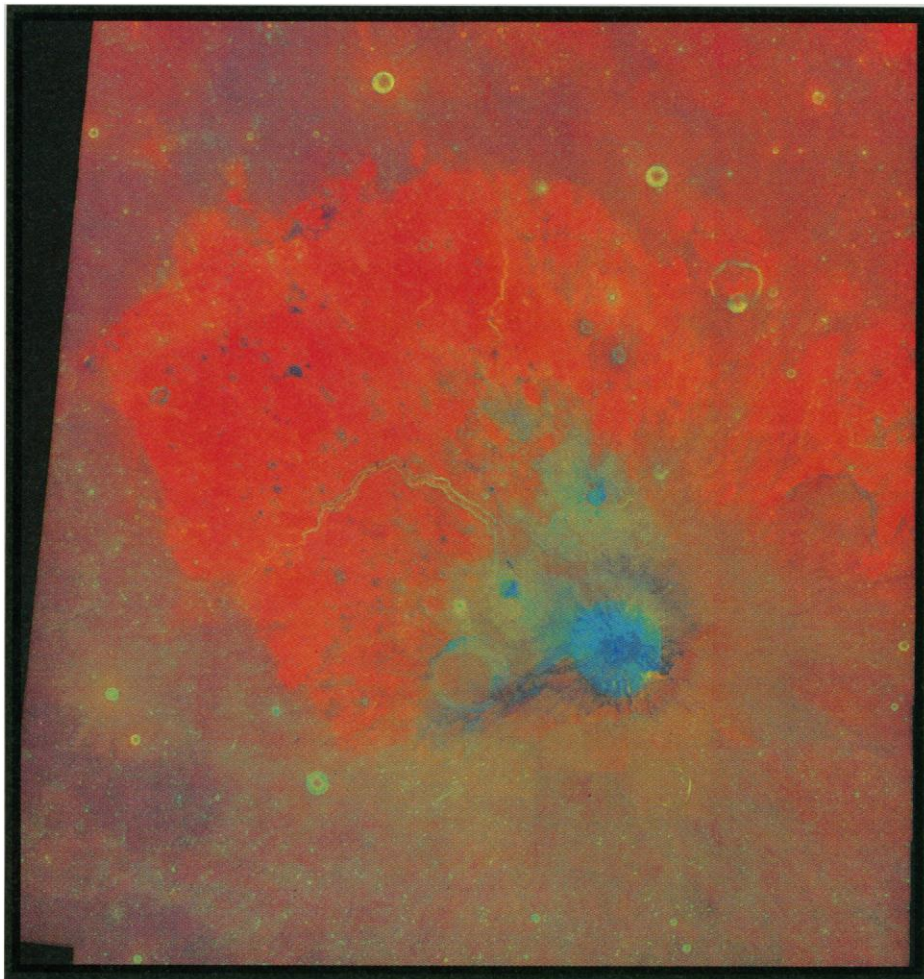


Fig. 2. Clementine altimetry profiles over the Aristarchus plateau. The lowest data point (bottom profile) is probably the floor of Aristarchus crater.

cept near the cobra head (which may be covered by highland ejecta from Aristarchus). The greenish color within craters and along rille walls (Fig. 3) indicates the presence of additional mare basalts over much of the plateau. Some of the mare exposures occur in smooth plains material that has embayed the hummocky highland materials on the plateau. This smooth plains material was previously thought to consist of either mare lavas or highland plains material (2, 3, 6); we now see that the plains unit is indeed mare basalt. Many craters and at least one rille also expose mare materials on generally hummocky terrains previously interpreted as highland materials (2, 3).

Many geologic mapping details will be revised after analysis of the Clementine data sets. One such example is provided by the Agricola Straits (Fig. 1), a low-lying zone that separates the plateau from the (apparently) fault-bounded Agricola Mountains to the northwest (2). The straits are composed of mare basalt and appear continuous in elevation with the mare fill surrounding the plateau (2, 3). However, the eastern half of the straits are largely covered by dark red material resembling the DMD (Fig. 3). Some of this red material may consist of red mare lavas, as appears to be the case in the western part of Agricola Straits, but the eastern straits have an especially low albedo and red color, like the DMD and unlike any nearby mare lavas. Thus, either the mare flows in Agricola Straits or the DMD must be subdivided into units of different ages.

The crater Aristarchus displays an interesting pattern of color and albedo units in its ejecta (Fig. 3) (3, 6, 19), which consists of both a discontinuous deposit that extends up to 300 km from the crater rim and a nearly contiguous high-albedo blanket around the crater, up to about 50 km from the rim. The Clementine mosaic (Fig. 3) confirms that the Aristarchus ejecta deposit is asymmetric; lobes of blue (highland) material extend north of the crater for ~100 km and west of the rim for ~75 km. The distribution of these lobes of highland composition is consistent with previous studies, suggesting excavation of such debris on the plateau side of the Aristarchus impact target (5, 6). On the mare side of the crater (east and south sectors), material near the crater rim consists of both blue (highland) units and well-exposed zones of a yellowish unit (probably mare basalt) at 2 and 4 o'clock. These yellowish areas correspond to the stripped zones described by Guest (5), in which late stage ejecta was thought to be removed from the near rim because it had high radial momentum after deposition. Outward 10 to 20 km from the rim, the intricately textured multicolor deposits sug-



**Fig. 3.** Color-ratio composite from UUVIS mosaic of 500 images in three spectral bands. The orthographic map projection covers 18°N to 32°N, 42°W to 57°W, at a scale of 100 m/pixel. The 750/415-nm ratio controls the red, the 750/1000-nm ratio controls the green, and the 415/750-nm ratio controls the blue.

gest basaltic ejecta mixed with highland debris and impact melt (5, 6). Mare basalt ejecta appears to be absent in the northwest sector of the crater ejecta blanket. A large streak of blue material (highland debris) extends up to 75 km southwest of the crater rim (Fig. 3); this streak could result from an asymmetric ejecta curtain or could be a consequence of ballistic shadowing by the plateau boundary fault exposed in this area (compare Fig. 1) or of reworking of highland materials in the plateau scarp.

We have processed four bandpasses of the NIR data in a north-south strip (orbit 186), which passes over the craters Aristarchus and Aristarchus A (Fig. 1). The NIR bandpasses are diagnostic of highland compositions because the 1100- and 2000-nm bands enable discrimination of olivine from pyroxene, and the 1250-nm band (compared with the 1500-nm continuum) is indicative of anorthite (16, 23). NIR color ratios (Fig. 4) enable us to map the distributions of compositional units. Pixel values from each bandpass were extracted

(Fig. 5) for two distinctive spectral features (see Fig. 4) and calibrated with coefficients for each of the bandpasses that were determined by dividing the Clementine data for Aristarchus A by the corresponding values in telescopic spectrum 1A of Lucey *et al.* (4). Two very bright areas (normal albedo ~0.5) on or near the central peak of Aristarchus have spectral values that match laboratory measurements of anorthite (23). A unit on the crater's south rim has spectral properties consistent with significant amounts of olivine, probably mixed with anorthite (that is, troctolite), as previously reported (4).

Anorthosite is not known elsewhere on the northwestern nearside of the moon. The presence of the 1250-nm anorthite band indicates that the bulk composition must be at least 85% anorthite, and the absence of a 1- $\mu$ m band indicates less than 5% pyroxene (24), so an anorthosite (>90% anorthite) classification is probably correct. Ferroan anorthosites are thought to have formed the primordial

**Fig. 4.** NIR coverage of Aristarchus crater from Clementine orbit 186. Arrows indicate the anorthositic central peaks (right center) and the olivine-rich unit on the crater rim (bottom right).

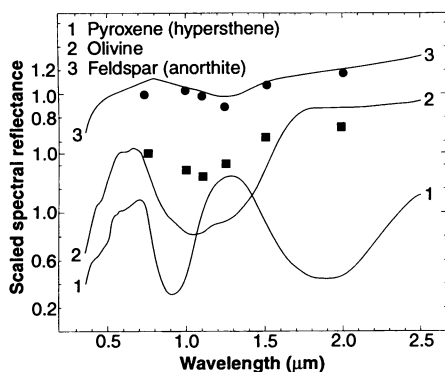
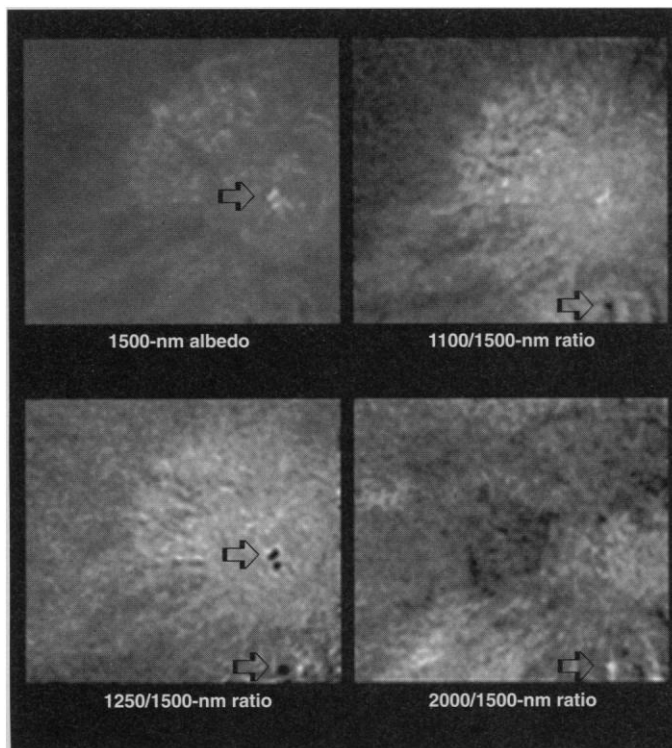


**Fig. 5.** Laboratory reflectance spectra of minerals commonly found in lunar highland rocks [from (23)], and Clementine reflectance data points for Aristarchus central peak bright spots (solid circles) and for a spot on the south rim of Aristarchus (solid squares; see Fig. 4 for locations).

lunar crust, emplaced as flotation cumulates in the global magma ocean (25). There has been much speculation about the asymmetric distribution of anorthosite on the moon's nearside. Wilhelms (26) proposed that the giant Procellarum impact event completely removed the primitive crust from this region. Other researchers favor an explanation involving enhanced magmatic intrusions and anorthosite assimilation in this region, due either to magma ocean processes or crustal thinning by single or multiple giant impacts (27, 28). Perhaps the anorthosite exposed in the uplifted central peak of

Aristarchus is a sample of more extensive primordial crust, largely buried by basin ejecta and mare lavas in this region of the moon. If so, then the presence of anorthosite at Aristarchus would argue against complete removal or assimilation of the primordial crust in this region.

An alternate possibility is that the Aristarchus central peak exposes an outcrop of alkalic anorthosite (29). Alkali anorthosites, rare in returned lunar samples, are richer in Na and K than the ubiquitous ferroan anorthosites and are extremely rich in incompatible elements (29). The only relatively large returned clast of alkali anorthosite (14047c) is relatively mafic-rich and lies along an extrapolation of Mg-suite compositional trends ( $Mg/[Mg + Fe]$  versus  $Ca/[Ca + Na + K]$ ). This sample also has rare-earth element (REE) concentrations ~40 times higher than that of the most REE-rich ferroan sample. Warren *et al.* (29) suggested that they may be late differentiates from Mg-suite magmatism that assimilated especially large amounts of urKREEP (residual liquid from the magma ocean, rich in potassium, REEs, phosphorus, and other incompatible trace elements). The alkali anorthosite interpretation for the Aristarchus central peaks is consistent with (i) high concentrations of KREEP (potassium, REE, phosphorus) and radioactive elements observed near Aristarchus crater from orbital gamma ray measurements (7); (ii) the fact that most of the few anorthosites from western landing sites are alkali, whereas all of the

pristine anorthosites from eastern sites are ferroan (29); and (iii) the evidence for voluminous post-magma-ocean magmatism in the Aristarchus region.

We have analyzed a tiny fraction of the global Clementine data set. The Aristarchus region covers less than one-half of 1% of the moon's surface, and we have analyzed only a portion of the Clementine data acquired of this region. The Aristarchus region is one of the better observed and studied regions of the moon, yet our brief study has resulted in improved knowledge of the topography, stratigraphy, and mineralogy of the region. Thus, this report is one small example of how the Clementine data set will improve our knowledge of the moon.

REFERENCES AND NOTES

1. S. Nozette *et al.*, *Science* **266**, 1835 (1994); E. M. Shoemaker, M. S. Robinson, E. M. Eliason, *ibid.*, p. 1851; M. T. Zuber and D. E. Smith, *ibid.*, p. 1839; P. G. Lucey, P. D. Spudis, M. Zuber, E. Malaret, *ibid.*, p. 1855; P. D. Spudis, R. A. Reisse, J. J. Gillis, *ibid.*, p. 1858; C. M. Pieters, M. I. Staid, E. M. Fischer, S. Tompkins, G. He, *ibid.*, p. 1844.
2. H. J. Moore, *U.S. Geol. Survey, Misc. Inv. Ser. Map I-465* (1965); *ibid.* I-527 (1967).
3. S. H. Zisk *et al.*, *Moon* **17**, 59 (1977).
4. P. G. Lucey, B. R. Hawke, C. M. Pieters, J. W. Head, T. B. McCord, *J. Geophys. Res.* **91**, D344 (1986).
5. J. E. Guest, *Geol. Soc. Am. Bull.* **84**, 2873 (1973).
6. \_\_\_\_\_ and P. D. Spudis, *Geol. Mag.* **122**, 317 (1985).
7. E. L. Haines, M. I. Etchegaray-Ramirez, A. E. Metzger, *Proc. Lunar Planet. Sci. Conf.* **9**, 2985 (1978).
8. W. S. Cameron, *NASA TM-X-65528* (1971).
9. P. Gorenstein and P. Bjorkholm, *Science* **179**, 792 (1973).
10. L. David, *Space News* **24** (13–19 June 1994).
11. M. J. Cintala, P. D. Spudis, B. R. Hawke, in *Lunar Bases and Space Activities of the 21st Century*, W. W. Mendell, Ed. [Lunar Planetary Institute (LPI), Houston, TX, 1985], pp. 223–237.
12. L. J. Friesen, *ibid.*, pp. 239–244.
13. L. R. Gaddis, C. M. Pieters, B. R. Hawke, *Icarus* **61**, 461 (1985).
14. G. H. Heiken, D. S. McKay, P. W. Brown, *Geochim. Cosmochim. Acta* **38**, 1703 (1974).
15. J. L. Whitford-Stark and J. W. Head III, *J. Geophys. Res.* **85**, 6579 (1980).
16. T. B. McCord *et al.*, *ibid.* **86**, 10883 (1981).
17. Defense Mapping Agency, *Lunar Topogr. Orthophotomap LAC 39* (1974).
18. M. J. S. Belton *et al.*, *Science* **264**, 1112 (1994).
19. T. V. Johnson, J. A. Mosher, D. L. Matson, *Proc. Lunar Planet. Sci. Conf.* **8**, 1013 (1977).
20. E. A. Whittaker, *Moon* **4**, 348 (1972).
21. R. A. F. Grieve, P. B. Robertson, M. R. Dence, in special issue entitled *Multi-Ring Basins*, P. H. Schultz and R. B. Merrill, Eds., *Proc. Lunar Planet. Sci.* **12A**, 37–58 (1981).
22. B. A. Campbell *et al.*, abstract in *Joint Workshop on New Technologies for Lunar Resource Assessment*, Santa Fe, NM, 6–7 April 1992 (LPI, Houston, TX, 1992), p. 8.
23. C. M. Pieters, *Rev. Geophys.* **24**, 557 (1986).
24. D. A. Crown and C. M. Pieters, *Icarus* **72**, 492 (1987).
25. J. V. Smith *et al.*, *Proceedings of the Apollo 11 Lunar Science Conference*, LPI, Houston, TX, 5–8 January 1970; A. A. Levinson, Ed. (Pergamon, New York, 1970), p. 897; J. A. Wood *et al.*, *ibid.*, p. 965.
26. D. E. Wilhelms, *U.S. Geol. Surv. Prof. Pap.* **1348** (1987).
27. P. G. Lucey and B. R. Hawke, *Proc. Lunar Planet. Sci. Conf.* **18**, 355 (1988).

28. P. H. Warren and G. K. Kallemeyn, *J. Geophys. Res.* **98**, 5445 (1993).
29. P. H. Warren, G. J. Taylor, K. Keil, *Proc. Lunar Planet. Sci. Conf. 13*, *J. Geophys. Res.* **88**, A615 (1983).
30. We thank K. Edwards, K. Becker, E. Lee, T. Becker, T. Sucharski, J. Mathews, D. Cook, D. McMacken, C. Bowers, and J. Torson [all with U.S. Geological Survey (USGS)]; E. Malaret and H. Taylor (Applied Coherent Technologies); and C. Acton (Jet Propulsion Laboratory) for contributions to the Clementine

data management and processing. Special thanks go to I. Lewis and H.-S. Park (Lawrence Livermore National Laboratory) for sensor calibrations and to T. Sorenson (AlliedSignal) and R. Reisse (Science Applications) for sequence planning. We also thank L. Gaddis (USGS), G. Blount (Texas A&M University), and two others for constructive reviews. This paper is LPI Contribution No. 848.

3 August 1994; accepted 1 November 1994

## An Alternative to SH2 Domains for Binding Tyrosine-Phosphorylated Proteins

W. Michael Kavanaugh and Lewis T. Williams\*

Src homology 2 (SH2) domains bind specifically to tyrosine-phosphorylated proteins that participate in signaling by growth factors and oncogenes. A protein domain was identified that bound specifically to the tyrosine-phosphorylated form of its target protein but differs from known SH2 sequences. Phosphotyrosine-binding (PTB) domains were found in two proteins: SHC, a protein implicated in signaling through Ras; and SCK, encoded by a previously uncharacterized gene. The PTB domain of SHC specifically bound to a tyrosine-phosphorylated 145-kilodalton protein. PTB domains are an alternative to SH2 domains for specifically recruiting tyrosine-phosphorylated proteins into signaling complexes and are likely to take part in signaling by many growth factors.

SH2 domains are amino acid sequences that are similar to a 100-residue noncatalytic region of the Src tyrosine kinase and are present in various signaling molecules (1). SH2 domains are functional protein motifs that bind tyrosine-phosphorylated targets by recognizing phosphotyrosine and specific adjacent residues (2). Activation of tyrosine kinases by growth factors, cytokines, and oncogenic agents therefore serves as a switch for assembling SH2 domain-containing proteins with their tyrosine-phosphorylated targets in signaling complexes in which downstream effectors are activated.

We identified a domain in the signaling protein SHC that binds specifically to the tyrosine-phosphorylated form of its target protein. The amino acid sequence of the PTB domain is not similar to that of any member of the known SH2 domain family. The SHC gene encodes 46- and 52-kD transforming proteins that are tyrosine phosphorylated in response to a number of growth factors and have been implicated as mediators of signaling from growth factor receptor and nonreceptor tyrosine kinases to Ras (3). The SHC protein contains (i) an SH2 domain at its COOH-terminus that binds tyrosine-phosphorylated targets such as activated growth factor receptors, (ii) a region of similarity to human alpha 1 collagen in the middle of the molecule that

contains a binding site for the GRB2 adapter protein, and (iii) a 232-residue NH<sub>2</sub>-terminus with no known function.

We investigated proteins that coimmunoprecipitated with SHC in growth factor-stimulated cells. Several tyrosine-phosphorylated proteins of approximately 145 kD (collectively called pp145) were present in anti-SHC immunoprecipitates from cells treated with either platelet-derived growth factor (PDGF) or fibroblast growth factor (FGF) but not in anti-SHC immunoprecipitates from unstimulated cells (Fig. 1). A similar tyrosine-phosphorylated protein or proteins were associated with SHC in B cells stimulated with antibodies to immunoglobulin M, in activated T cells, in HepG2 hepatoma cells stimulated with interleukin-6, and in CCE embryonic stem cells stimulated with leukemia inhibitory factor (4). The number and electrophoretic mobility of the pp145 proteins varied slightly among different cell types. These may represent different proteins or the same protein with different amounts of phosphorylation. All of these proteins appear to bind to SHC in a similar manner. The pp145 proteins in fibroblasts or in B cells were not recognized by immunoblotting with antibodies to SHC, phospholipase C gamma, Ras guanosine triphosphatase-activating protein, the guanine nucleotide exchange factor Son of Sevenless (SOS), insulin receptor substrate 1, the guanine nucleotide exchange factor C3G, the transforming protein Eps 15, or the PDGF or FGF receptors (5).

To characterize binding of SHC to

pp145, we separated proteins from cell lysates by SDS-polyacrylamide gel electrophoresis (SDS-PAGE), transferred them to nitrocellulose, and incubated them with <sup>32</sup>P-labeled glutathione-S-transferase (GST)-SHC fusion protein. <sup>32</sup>P-labeled SHC bound specifically to three proteins of approximately 180, 145, and 120 kD from lysates of PDGF-stimulated fibroblasts but did not bind any proteins from lysates of unstimulated cells (Fig. 2A). The 180-kD band comigrated with the autophosphorylated PDGF receptor; the 145-kD band comigrated with the major pp145 protein identified in Fig. 1; the identity of the 120-kD protein is unknown. The <sup>32</sup>P-SHC probe also bound 145-kD proteins present in anti-SHC immunoprecipitates from PDGF-stimulated cells but did not bind any proteins in immunoprecipitates from unstimulated cells (Fig. 2A). Therefore, the <sup>32</sup>P-SHC probe apparently binds to the same 145-kD protein or proteins that associate with SHC in vivo. These experiments demonstrate that SHC binds pp145 directly and that interaction of SHC and p145 in vitro requires PDGF stimulation in vivo.

To map the region of SHC responsible for binding to pp145, <sup>32</sup>P-SHC probes were prepared that contained deletions of various domains. Deletion of the SH2 domain of SHC eliminated binding to the p180 and p120 proteins in lysates of PDGF-stimulated cells but did not affect binding to pp145 in either cell lysates or in anti-SHC immunoprecipitates (Fig. 2B). Further, the isolated SH2 domain from SHC bound to p180 and p120 but not to pp145 (Fig. 2B).

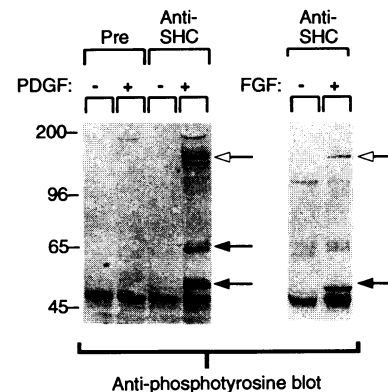


**Fig. 1.** Association of SHC with 145-kD tyrosine-phosphorylated proteins in vivo. Balb/3T3 fibroblasts were stimulated with PDGF (left); L6 myoblasts expressing the human FGF receptor 1 were stimulated with bFGF (right) (12). Cell lysates were immunoprecipitated with preimmune serum or antiserum to SHC and immunoblotted with antibody to phosphotyrosine. Black arrows indicate the 52-kD SHC protein and a 66-kD SHC-related protein seen in fibroblasts. The pp145 proteins are indicated by open arrows. Each lane contains equal amounts of SHC, as determined by immunoblotting with antiserum to SHC (5).

Cardiovascular Research Institute, Department of Medicine, University of California, San Francisco, CA 94143, USA.

\*To whom correspondence should be addressed.